SUPPORTING INFORMATION FOR

Chiral Guided Mode Resonance with Independently Controllable Quality Factor and Circular Dichroism

Zhancheng Li, [†] *Shiwang Yu,* [†] *Guangzhou Geng,* [‡] *Jiaqi Cheng,* [†] *Wenwei Liu,* [†] *Yuebian Zhang,* [†] *Junjie Li,* [‡] *Hua Cheng,* [*,†] *and Shuqi Chen* [*,†,¶,§]

[†] The Key Laboratory of Weak Light Nonlinear Photonics, Ministry of Education, School of Physics and TEDA Institute of Applied Physics, Nankai University, Tianjin 300071, China

[‡] Beijing National Laboratory for Condensed Matter Physics, Institute of Physics, Chinese Academy of Sciences, Beijing 100190, China

[¶] School of Materials Science and Engineering, Smart Sensing Interdisciplinary Science Center, Nankai University, Tianjin 300350, China

[§] The Collaborative Innovation Center of Extreme Optics, Shanxi University, Taiyuan, Shanxi 030006, China

[*] Corresponding author: hcheng@nankai.edu.cn and schen@nankai.edu.cn

Section 1. Analysis on the circular dichroism (CD) of the excited resonances in the wavelength region of interest.

To show the chiral of folded bands 1 to 5, we simulated the transmittance-momentum spectra of the designed metasurface grating with $\delta_d = 20$ nm under left-handed circularly polarized (LCP) and right-handed circularly polarized (RCP) incidence and calculated the corresponding CD-momentum spectra, as shown in Figure S1. The results presented in Figure S1 align well with those in Figures 3(a) and 3(b), confirming that the resonance mode of band 3 is a leaky mode characterized by a low Q factor, while the resonance modes of bands 2 and 4 are symmetry-protected bound states in the continuum (BICs). The results also indicate that the modes of the folded bands 1 to 5 are all chiral modes, each exhibiting different values of CD. Moreover, band 1 in Figures 3(a) and 3(c) displays a flat band for $|k_x| < 0.0115$. This flat band is truncated due to the emergence of diffraction channels when $|k_x|$ larger than 0.0115, corresponding to an incident angle of 0.92 degrees, as illustrated in Figure S1(b).

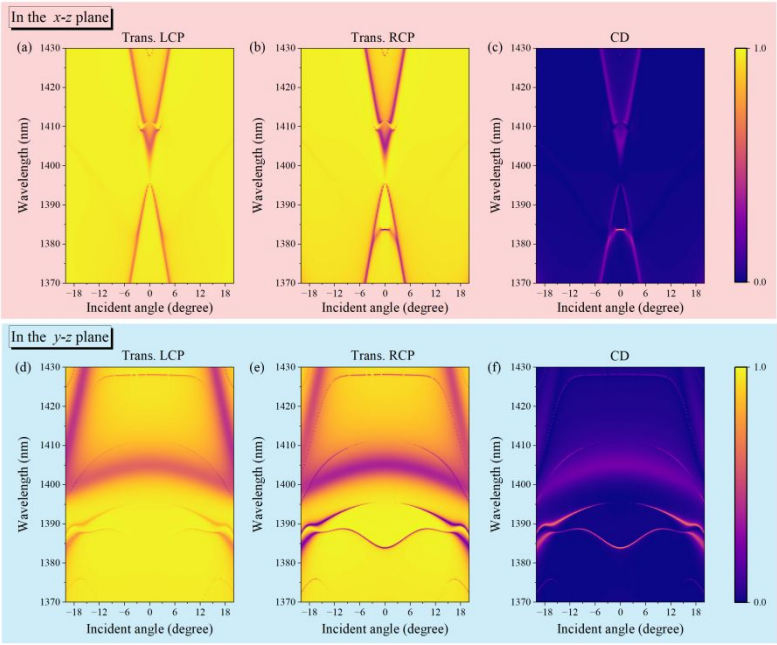

Figure S1. Transmittance-momentum spectra of the designed metasurface grating with $\delta_d = 20$ nm under LCP and RCP incidence and the corresponding CD-momentum spectra. Transmittance-momentum spectra under (a) LCP and (b) RCP incidence in the *x*-*z* plane, and (c) the corresponding CD-momentum spectrum. Transmittance-momentum spectra under (d) LCP and (e) RCP incidence in the *y*-*z* plane, and (f) the corresponding CD-momentum spectrum.

Section 2. Calculated guided mode fields under LCP and RCP normal illumination based on collective interference model.

Since LCP and RCP waves can be decomposed into transverse electric (TE) and transverse magnetic (TM) components with a phase delay of ±π/2 (Figure 3(d)), the phase difference between the guided mode fields excited by the TM and TE components of LCP and RCP waves is π and 0, respectively, resulting in destructive and constructive interference. Consequently, the coupling strength (quantitatively described by $|E_z|$) of the GMR under LCP and RCP illumination is eliminated and enhanced, respectively. Specifically, the $|E_z|$ of the excited guided mode fields at the middle cross-section of the planar thin slab under LCP and RCP illumination can be obtained based on the equations $|E_z^{TM}(1+E_z^{TE}/E_z^{TM})|$, where E_z^{TE} and E_z^{TM} represent E_z of the guided mode fields excited by the TE and TM components of the LCP and RCP waves. As shown in Figure S2, the calculated results are in good agreement with the simulated ones in Figure 3(e).

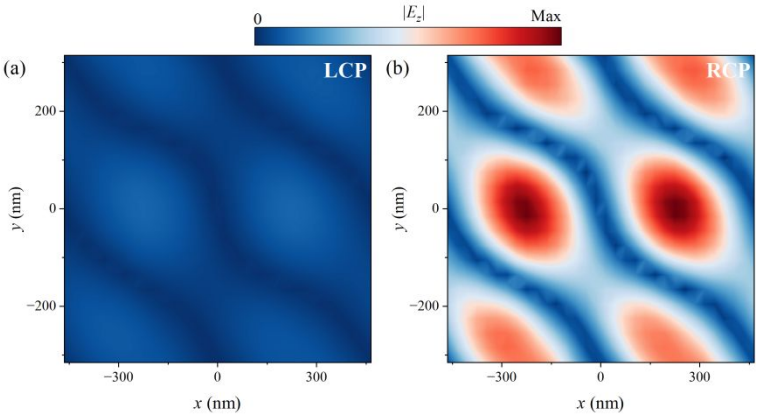

Figure S2. Calculated distributions of the magnitude of the *z*-component of the electric field on the middle cross section of the *α*-Si slab under LCP and RCP normal incidence.

Section 3. The variation in coupling strength between the guided mode resonance (GMR) and both the TE and TM normal incidence, as well as the resonant wavelength, as a function of δ_d and P_y.

To show the variation of coupling strength between the GMR and both the TE and TM normal incidence, we calculated the variation of the mean values of the amplitude of the *z*-component of the electric field (E_z) at the middle cross-section of the α-Si slab under normal incidence of TE and

TM waves at the resonant wavelength as a function of δ_d and P_y, as shown in Figure S3. Results indicate that the coupling strength between the GMR and the TE and TM normal incidence decrease with increasing δ_d, while their ratio remains relatively constant. In contrast, the coupling strength between the GMR and TE waves initially increases and then decreases with variations in P_y, whereas the coupling strength between the GMR and TM waves continues to increase with changes in P_y, leading to a variation in their ratio. Moreover, the resonant wavelength of the GMR slightly redshifts with increasing P_y, while it remains constant with variations in δ_d, as illustrated in Figure S4.

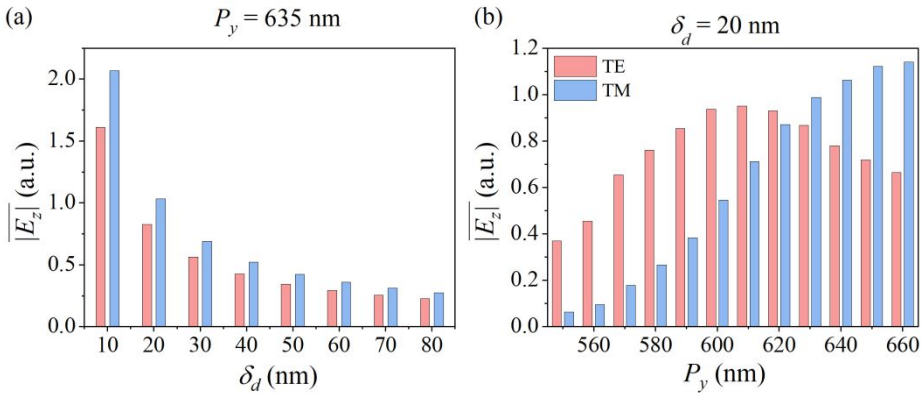

Figure S3. Calculated variation of the mean values of the amplitude of the *z*-component of the electric field (E_z) at the middle cross-section of the α-Si slab under normal incidence of TE (*y*-polarized) and TM (*x*-polarized) waves at the resonant wavelength as a function of (a) δ_d and (b) P_y, respectively.

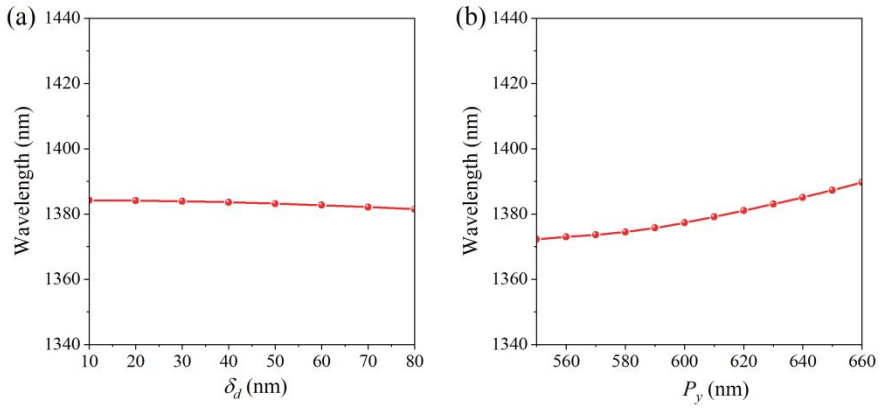

Figure S4. The variation of resonant wavelength with changing (a) δ_d and (b) P_y.

Section 4. Variation of CD spectrum with the changing of structural parameters

To demonstrate how changes in structural parameters affect the CD of the GMR, we simulated the variation of the CD spectrum with several structural parameters, as shown in Figure S5. The results indicate that the thickness of the planar thin slab significantly influences the resonant wavelength due to the inherent properties of GMR. Additionally, the CD and Q factor of GMR remain relatively stable with variations in the structural parameters of the Z-shaped nanostructures. An increase in l_1 and l_2 leads to a small redshift of the resonant wavelength, while the CD remains constant, allowing for further adjustments to the resonant wavelength when P_y is modulated.

We further analyze the effect of changing the distance between the Z-shaped nanostructures along the *y*-direction on the CD spectrum. Modifying the distance between the two Z-shaped nanostructures along the *x*-direction has two main effects: (1) it causes Brillouin zone folding along the k_x-direction, leading to the excitation of GMR, and (2) it alters the radiation loss of the GMR, resulting in a variation of the Q factor. When the distance between the Z-shaped nanostructures along the *x*-direction is set to $P_x/2$, changing the distance between the adjacent nanostructures along the *y*-direction causes Brillouin zone folding along the k_y-direction. However, due to the small structural period along the *y*-direction, no guided modes exist within the waveband of interest (1370 nm–1450 nm, as investigated in Figure 3(a)). As a result, no GMR is observed in this range. GMR due to Brillouin zone folding along the k_y-direction can only be observed at shorter wavelengths. On the other hand, when the distance d_y between the two adjacent Z-shaped nanostructures along the *y*-direction is modified, while the distance between the nanostructures along the *x*-direction is not equal to $P_x/2$, GMR caused by Brillouin zone folding along the k_x-direction can be observed. We further simulated the variation of the CD spectrum as a function of δ_{dy} (defined as $P_y–d_y$) when δ_d = 20 nm as illustrated in Figure S6. The results indicate that an increase in δ_{dy} leads to a slight redshift of the resonant wavelength, while the Q factor and CD of the GMR remain almost unchanged. Since the distance between the two adjacent Z-shaped nanostructures is quite small, the shift in the resonant wavelength can be attributed to the enhanced near-neighbor coupling between the nanostructures along the *y*-direction.

It should be noted that the structural symmetry of the Z-shaped nanostructures also plays a key role in the realization of chiral GMR. Variations in structural symmetry alter the collective

interference effect and, consequently, change the CD spectrum, as validated in Figure S7. Specifically, when the Z-shaped nanostructures are replaced with cross-shaped nanostructures, the GMR can only be excited under TE illumination, resulting in the disappearance of the chiroptical response. Interestingly, the Q factor of the GMR remains almost unchanged with variations in the structural symmetry parameter $\delta_{str.}$. Therefore, modulation of structural symmetry provides an alternative approach for CD manipulation.

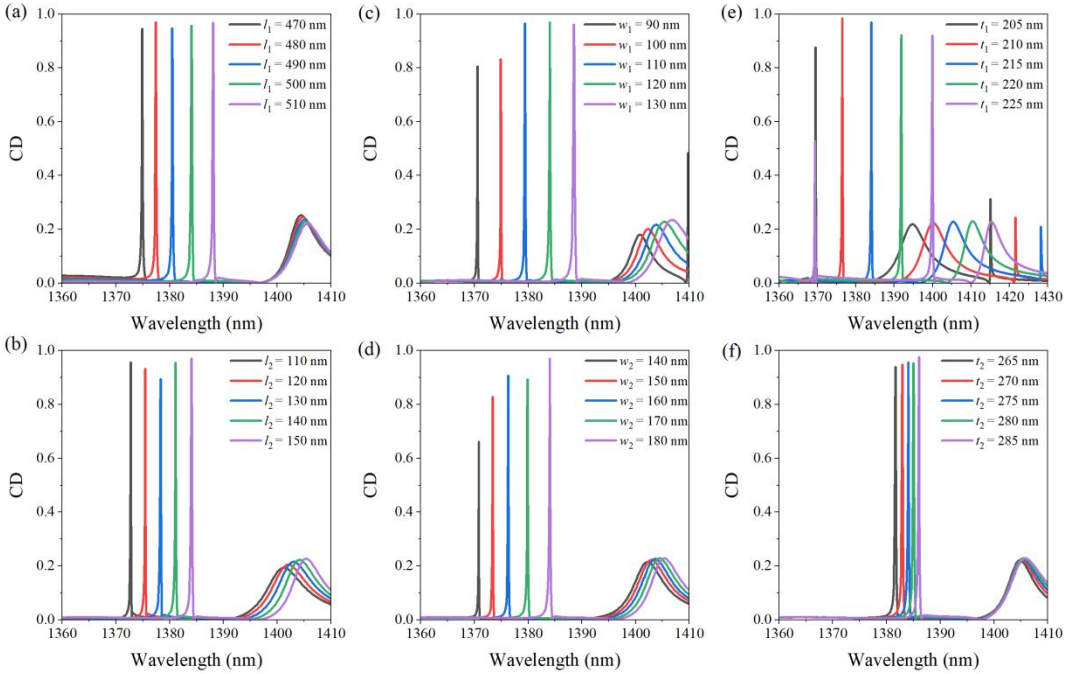

Figure S5. Variation of CD spectrum with the changing of structural parameters: (a) l_1, (b) l_2, (c) w_1, (d) w_2, (e) t_1, (f) t_2.

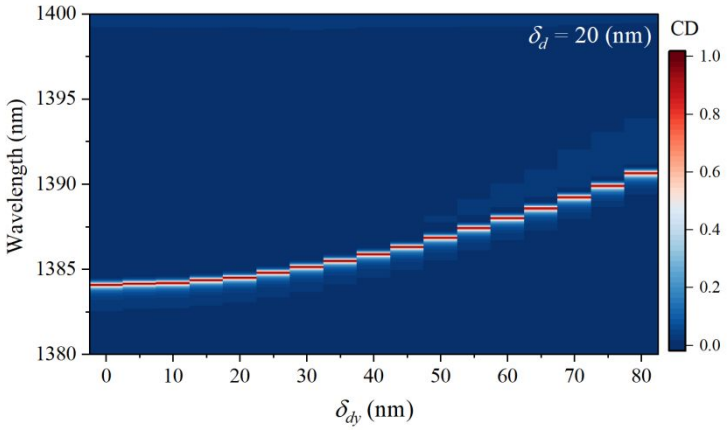

Figure S6. Simulated CD-δ_{dy} spectra of the designed metasurface grating when δ_d = 20 nm.

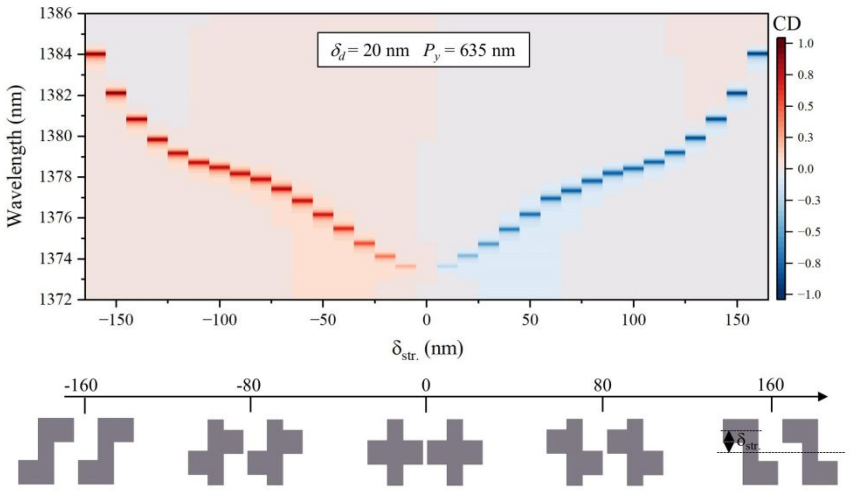

Figure S7. (Upper layer) Simulated CD-$\delta_{str.}$ spectra of the designed metasurface grating when δ_d = 20 nm. (Bottom layer) The definition of structural symmetry parameter $\delta_{str.}$ and the nanostructures comprising the metasurface gratings with different values of $\delta_{str.}$.

Section 5. Validation of the independent manipulation of the Q factor and CD of the chiral GMR by changing δ_d and P_y

To further demonstrated that the Q factor and CD of the chiral GMR can be independently manipulated by changing δ_d and P_y respectively, we simulated the variation of the Q factor, CD and resonant wavelength of the chiral GMR with the changing of δ_d and P_y, as illustrated in Figure S8. The results validate that the Q factor and CD of the chiral GMR can indeed be independently controlled by changing δ_d and P_y respectively.

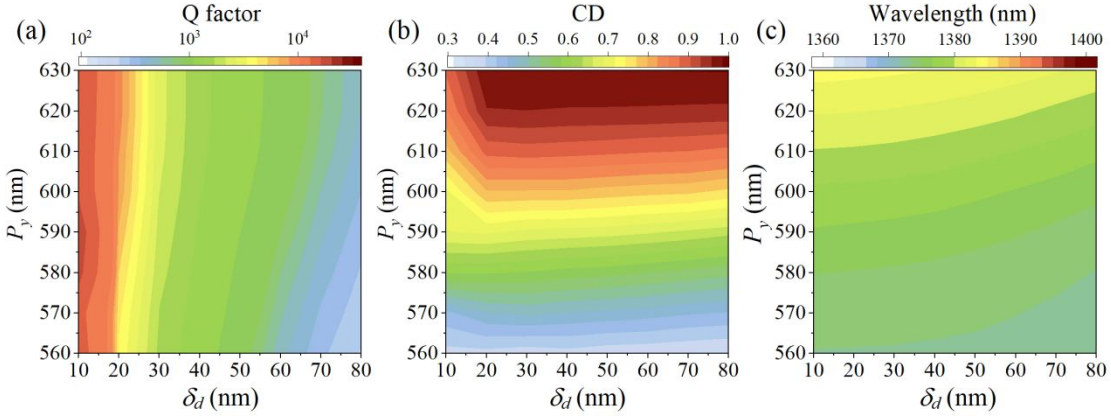

Figure S8. Simulated results of the variation of the (a) Q factor, (b) CD and (c) resonant wavelength of the chiral GMR with the changing of δ_d and P_y.

Section 6. Details of sample fabrication and transmission spectra measurement

Sample fabrication: The designed metasurfaces, composed of amorphous silicon (α-Si) Z-shaped nanostructures and a thin slab, were fabricated on a fused quartz substrate using plasma-enhanced chemical vapor deposition (PECVD), electron beam lithography, electron beam evaporation, and plasma reactive ion etching (RIE). First, an α-Si film with a thickness of 490 nm was deposited on the fused quartz substrate via PECVD. Next, a layer of polymethyl methacrylate (PMMA) resist 950-A7 was spin-coated onto the α-Si film and patterned using electron beam lithography. A 100 nm thick chromium (Cr) layer was then deposited via electron beam evaporation. After a lift-off process to remove unpatterned areas, the designed structures were transferred from the chromium to the α-Si through plasma RIE. The partial etching depth (275 nm) was precisely controlled by adjusting the RIE duration, maintaining a constant etching rate of 3 nm/sec. Finally, the residual Cr was removed by cerium (IV) ammonium nitrate.

Experimental Measurement: The transmission spectra of the designed metasurfaces were measured using a custom-built optical setup. A super-continuum laser (SuperK, EXR-20) served as the broadband light source. The laser beam first passed through a broadband polarizer (Codixx AG, IR 1300 BC5) and an achromatic quarter-wave plate (B. Halle Nachfl, λ/4 super achromatic waveplate) to generate a circularly polarized beam. This beam then illuminated the sample, and the transmitted beam was collected using an objective lens (Sigma NIR Plan Apo 20×, NA = 0.45). The collected beam passed through another achromatic quarter-wave plate (B. Halle Nachfl, λ/4 super achromatic waveplate) and another broadband polarizer (Codixx AG, IR 1300 BC5), followed by an aperture and a lens, and was then collected by an optical spectrum analyzer (Zolix, Omni-750i) via a fiber coupler. The polarizer and quarter-wave plate positioned after the objective lens were employed to acquire the two orthogonal circularly polarized components of the transmitted beam. The aperture controlled the measurement area, making it slightly smaller than the size of the sample. A switchable mirror was placed behind the lens to switch between sample imaging, captured by a CMOS camera (TUCSEN, Mlchrome 5BW), and spectral measurement. The data of transmission intensity was acquired with the software of the optical spectrum analyzer. The collected data were normalized by dividing them with the background spectrum of air in order to obtain the transmission spectra.